A single image dehazing method based on decomposition strategy

QIN Chaoxuan[1,2] and GU Xiaohui[1,*]

1. School of Mechanical Engineering, Nanjing University of Science and Technology, Nanjing 210094, China;
2. Southwest Technology and Engineering Research Institute, Chongqing 400039, China

Abstract: Outdoor haze has adverse impact on outdoor image quality, including contrast loss and poor visibility. In this paper, a novel dehazing algorithm based on the decomposition strategy is proposed. It combines the advantages of the two-dimensional variational mode decomposition (2DVMD) algorithm and dark channel prior. The original hazy image is adaptively decomposed into low-frequency and high-frequency images according to the image frequency band by using the 2DVMD algorithm. The low-frequency image is dehazed by using the improved dark channel prior, and then fused with the high-frequency image. Furthermore, we optimize the atmospheric light and transmittance estimation method to obtain a defogging effect with richer details and stronger contrast. The proposed algorithm is compared with the existing advanced algorithms. Experiment results show that the proposed algorithm has better performance in comparison with the state-of-the-art algorithms.

Keywords: single image dehazing, decomposition strategy, image processing, global atmospheric light.

1. Introduction

The presence of outdoor haze normally reduces image quality captured by imaging devices, leading to contrast loss and distorted colors. Therefore, improving the image dehazing technology is of great significance in both military and civilian fields. This technology is applied in numerous fields, including aerial imagery, video surveillance, image guidance recognition, and automatic driving. It is also a hot issue in computer vision.

Image dehazing methods are mainly divided into the multi-image and the single-image dehazing methods. The previous image dehazing algorithms estimates image depth information from multiple images and restore the images. However, it is difficult to obtain multiple images in practice. Schechner et al. [1] proposed an image defog-

ging method based on polarization, which utilized two images in different directions to reversely push the image degradation process for defogging. Other scholars [2−4] achieved remarkable improvements based on the Schechner's method. However, as the degree of polarization decreases, the efficiency of the method decreases and the algorithm fails if the camera moves. Miyazaki et al. [5] captured images in different climates to recover the real scene information and this algorithm had a good performance on fixed cameras such as monitoring scenes. However, it is almost impractical to obtain images of the same scene for moving cameras on different climatic conditions. Therefore, the research focus has recently shifted to the dehazing of a single image. The single-image dehazing method can be more feasible with greater practical values in comparison with the multi-image dehazing method.

The single-image dehazing algorithm is mainly divided into three categories, image-enhancement-based algorithms, image-restoration-based algorithms, and deep-learning based algorithms. The image enhancement method does not concern the cause of the image degradation. Moreover, it improves image quality in accordance with the image information only, and suppresses or removes unnecessary information of the image to promote the image quality. It applies different techniques, including image wavelet transform [6−8], image filtering [9−11], histogram equalization [12], and the Retinex based algorithm [13−15]. However, the image-enhanced algorithm is less robust, because it does not mention the cause of the image degradation.

Based on the image restoration algorithm, the physical model of the image degradation is established. Considering the cause of the foggy image degradation, the atmospheric scattering model is applied to solve the relevant parameters. Then, the real scene image is restored using estimation of atmospheric light and transmission. Fattal [16] put forward the atmospheric transport model and pro-

posed a method for estimating the global atmospheric light and the transmission. Although this method estimates the atmospheric light and transmission reasonably, it is less effective when the signal-to-noise ratio is insufficient or the fog is too thick. Tan [17] proposed a method for images with the following two characteristics. Firstly, the fog-free image should have a higher contrast than the foggy images. Secondly, the light variation should depend on the distance from the object to the camera, and the corresponding light variation in a small range should be low and smooth. For images in these circumstances, he established the cost function in the Markov random domain. Then the image was restored. However, this method had some disadvantages, for example, the image may be supersaturated with a halo phenomenon. He et al. [18] proposed the dark channel prior model, which has received extensive attention and be applied broadly. With careful observation, it has been found that fog-free images usually have a channel whose pixel value approaches 0. This method was used to estimate the transmission to recover the images. Then the guide filtering algorithm [19] was proposed to solve the problems of large computation and halo phenomenon existing in the soft matting algorithm of the dark channel prior. Many scholars conducted relevant researches on the basis of dark channel prior. Tarel et al. [20] applied the median filtering instead of the soft stencil and proposed a fast-dehazing algorithm to improve the algorithm efficiency. The computational load has a linear correlation with the image size, which significantly improves computational efficiency [20]. However, the median filtering has poor retention of the edges and the atmosphere estimation hardly reflects depth information. Moreover, it is a challenge to achieve the expected effect for small edge regions with large jumps.

In the studies of the dark channel theory, scholars usually optimized the estimation of the atmospheric light and the calculation of the transmission. Wang et al. [21] proposed a differential algorithm to estimate the atmospheric light and optimize the calculation method of the transmission, while the image was too bright. Huang et al. [22] calculated the transmission for bright and non-sky areas, including white clouds. However, the algorithm did not have reasonable performance in the dark area. Peng et al. [23] investigated variations of the depth-related color to estimate the ambient light and achieve better visual effects. Wang et al.[24] combined the variational model and the dark channel prior model to suppress the noise originated from the image dehazing.

With the recent development of the deep learning technology, learning-based dehazing methods have also been proposed [25,26]. In recent years, deep learning-based defogging methods have gradually become a hotspot in the field of image defogging. The earliest deep learning-

defogging network is the DehazeNet proposed by Cai et al. [27], which estimated the transmittance by deep learning methods for the first time. The network divides the complete image into blocks, input the image blocks with fog, and output the transmittance of the corresponding blocks for image restoration using the atmospheric scattering model. Ren et al. [28] proposed multi-scale convolutional neural networks (MSCNN), a model from coarse-scale network to fine-scale network which estimated the transmittance by learning so as to achieve fog removal. Li et al. [29] designed the all-in-one dehazing network (AOD-Net) based on a reformulated atmospheric scattering model. Instead of estimating the transmission matrix and the atmospheric light separately, AOD-Net directly generated the clean image through a light-weight CNN. Deep learning methods are limited by the size and quality of existing defogging data sets, so it is difficult for the trained models to steadily output high quality defogging results in real scenes.

Our goal is to obtain a dehazing effect with higher contrast and retain richer image details. We find that the frequency components of images polluted by haze will become lower. Therefore, this paper decomposes the original hazy image into a low-frequency image and a high-frequency image. The haze information is all centered on the low-frequency image. The high-frequency images contain detailed texture information. The low-frequency image is dehazed, and then fused with the high-frequency images. Furthermore, we optimize the atmospheric light and transmittance estimation method to obtain a defogging effect with richer details and higher contrast.

The contributions of the present study are summarized as follows:

(i) This paper proposes an image defogging algorithm based on decomposition strategy, which combines 2DVMD and improved dark channel prior algorithm.

(ii) A new method is proposed for the atmospheric light estimation, which uses different atmospheric light estimation methods for the sky and the non-sky images.

(iii) The hazy image is adaptively decomposed into low-frequency and high-frequency images according to the image frequency band. Next, a more detailed and higher contrast dehazing effect can be achieved by dehazing the low-frequency image and then fusing with the high-frequency image.

The rest of this paper is structured as follows: the proposed method is discussed in Section 2, the experimental results are illustrated in Section 3, and Section 4 presents the conclusions of this paper.

2. Methods

We find that the frequency components of images polluted by haze will become lower, and the frequency com-

ponents of images are mostly concentrated in the low-frequency part, while the high-frequency distribution is very small, as shown in Fig. 1. Thus, the basic idea of this paper is to extract the low frequency components of the hazy images. The haze information is contained in the low-

frequency components and the detailed texture information is included in the high frequency components. Therefore, we restore the low frequency components and then fuse them with the high frequency parts and finally get high contrast processing results with good visual effects.
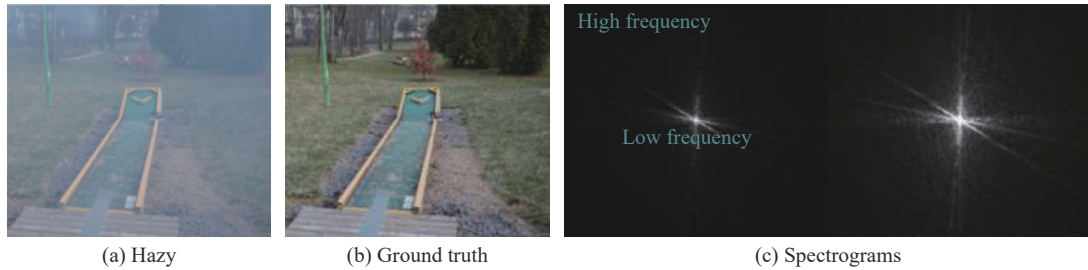

| (a) Hazy | (b) Ground truth | (c) Spectrograms |

Fig. 1   Frequency spectrum of haze image and hazefree image

The algorithm flow chart of this paper is shown in Fig. 2. Firstly, the original foggy image is decomposed into several intrinsic mode functions (IMFs) through the 2DVMD algorithm.

$$I(x,y) = I_{\text{IMF1}} + I_{\text{IMF2}} + \cdots + I_{\text{IMF}n} \tag{1}$$

where I_{IMF1} denotes the low frequency component of the original hazy images and $I_{\text{IMF2}}, I_{\text{IMF3}}, \cdots, I_{\text{IMF}n}$ stands for high components. Next, since the hazy information is included in the low-frequency IMF component, the low-frequency component is optimized by the improved dark

channel algorithm. For sky-included images, the sky segmentation algorithm is applied to estimate the atmospheric light while for non-sky images, the quad-tree search algorithm is adopted to search global atmospheric light. The context information constructor is combined to optimize the transmission so that the atmospheric light and the transmission can be employed to generate fog-free images. Finally, fused with the high frequency components, a high contrast, good visual effects, and haze-free image is obtained. The program flowchart of the proposed method is shown in Fig. 2.
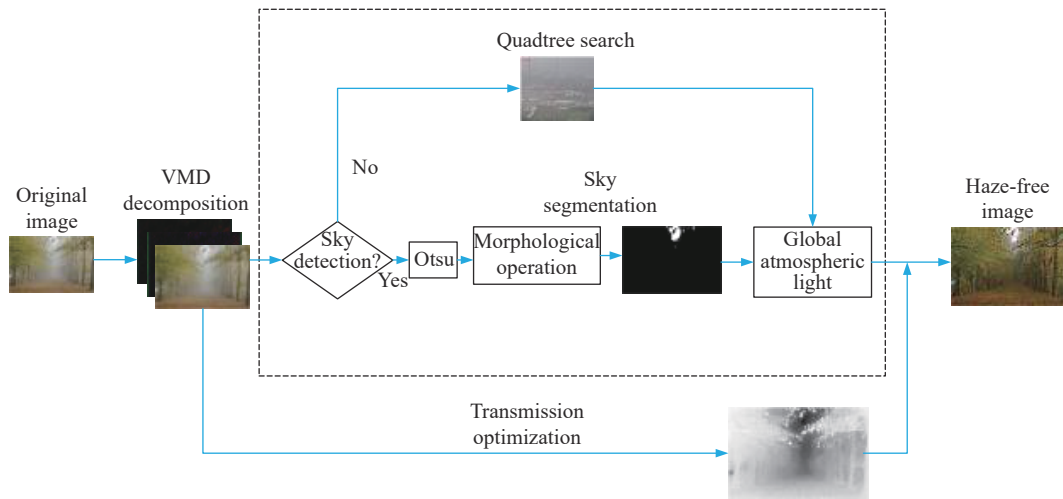

Fig. 2   Flowchart of the proposed method

2.1   Hazy image adaptively decomposed

The variational mode decomposition (VMD) algorithm is suitable for processing nonlinear and non-stationary signals, decomposing the original signal into modes with a center frequency and limited bandwidth, and has strong adaptability [30]. Here we use the idea of VMD. 2DVMD

is an extension of VMD. The 2D signals can be defined in the frequency domain as follows:

$$\boldsymbol{u}_{AS,k}(\boldsymbol{w}) = \begin{cases} 2\hat{\boldsymbol{u}}_k(\boldsymbol{w}), & \boldsymbol{w}\boldsymbol{w}_k > 0 \\ \hat{\boldsymbol{u}}_k(\boldsymbol{w}), & \boldsymbol{w}\boldsymbol{w}_k = 0 \\ \boldsymbol{0}, & \boldsymbol{w}\boldsymbol{w}_k < 0 \end{cases}. \tag{2}$$

Assume that each mode has a center frequency and a finite bandwidth. The two-dimensional VMD problem is transformed into a K mode function problem $\boldsymbol{u}_k$. Based on the characteristics of the Fourier transform, (2) can be rewritten as

$$\boldsymbol{u}_{AS,k}(\boldsymbol{x}) = \boldsymbol{u}_k(\boldsymbol{x}) * \left[\delta(\langle \boldsymbol{x}, \boldsymbol{w}_k\rangle) + \frac{j}{\pi\langle \boldsymbol{x}, \boldsymbol{w}_k\rangle}\right]\delta(\langle \boldsymbol{x}, \boldsymbol{w}_k^\perp\rangle) \quad (3)$$

where $*$ is the convolutional operator and $\boldsymbol{w}$ is the instantaneous frequency of the mode function transforming $\boldsymbol{u}_k$ into the frequency domain, and $\boldsymbol{u}_k$ is the constituent element of the decomposed image that we obtain, j is the imaginary part of the Fourier domain. $\boldsymbol{w}_k$ denotes the frequency interface of the kth selected mode when the frequency domain half plane is set to 0. $\boldsymbol{w}_k^\perp$ is a unit vector which is orthogonal to $\boldsymbol{w}_k$: $\boldsymbol{w}_k \cdot \boldsymbol{w}_k^\perp = 0$. $\delta(\cdot)$ is the Dirac equation. The variational mode decomposition can keep each mode to be concentrated around the center frequency $\boldsymbol{w}_k$, where the central frequency and mode components can be obtained by minimizing a functional which can be expressed as

$$\min_{\boldsymbol{u}_k,\boldsymbol{w}_k}\left(\sum_k \left\|\nabla(\boldsymbol{u}_{AS,k}(\boldsymbol{x})\mathrm{e}^{-\mathrm{j}\langle \boldsymbol{x},\boldsymbol{w}_k\rangle})\right\|_2^2\right)$$
$$\text{s.t.} \sum_k \boldsymbol{u}_k = \boldsymbol{I}. \quad (4)$$

The solution of (4) can be transformed into an unconstrained variational solution problem by constructing an augmented Lagrange function.

$$L(\{\boldsymbol{u}_k\},\{\boldsymbol{x}_k\},\lambda) =$$
$$\sum_k a_k \left\|\nabla(\boldsymbol{u}_{AS,k}(\boldsymbol{x})\mathrm{e}^{-\mathrm{j}\langle \boldsymbol{x},\boldsymbol{w}_k\rangle})\right\|_2^2 +$$
$$\left\|\boldsymbol{I} - \sum_k \boldsymbol{u}_k\right\|_2 + \left\langle\lambda(\boldsymbol{x}), \boldsymbol{I} - \sum_k \boldsymbol{u}_k\right\rangle \quad (5)$$

where λ and a_k denote the Lagrange multipliers and the corresponding penalty factors, respectively. Applying alternating direction multipliers results in the following:

$$\hat{\boldsymbol{u}}_k^{n+1} = \arg\min_{\hat{\boldsymbol{u}}_k} \left\{a\left\|\mathrm{j}(\boldsymbol{w}-\boldsymbol{w}_k)\cdot\right.\right.$$
$$\left.[(1+\mathrm{sgn}(\boldsymbol{w}\cdot\boldsymbol{w}_k))\boldsymbol{u}_k(\boldsymbol{w})]\right\|_2^2 +$$
$$\left.\left\|f(\boldsymbol{w}) - \sum_k \boldsymbol{u}_i(\boldsymbol{w}) + \frac{\lambda(\boldsymbol{w})}{2}\right\|_2^2\right\}, \quad (6)$$

$$\hat{\boldsymbol{w}}_k^{n+1} = \arg\min \{a\|\mathrm{j}(\boldsymbol{w}-\boldsymbol{w}_k)[(1+$$
$$\mathrm{sgn}(\boldsymbol{w}\cdot\boldsymbol{w}_k))\boldsymbol{u}_k(\boldsymbol{w})]\|_2^2\}. \quad (7)$$

The foregoing equations can be simplified in the following form:

$$\hat{\boldsymbol{u}}_k^{n+1} = \frac{\left(\hat{\boldsymbol{I}}(\boldsymbol{w}) - \sum_{i\neq k}\hat{\boldsymbol{u}}_i(\boldsymbol{w}) + \frac{\lambda(\boldsymbol{w})}{2}\right)}{1+2a|\boldsymbol{w}-\boldsymbol{w}_k|^2},$$
$$\forall \boldsymbol{w} \in \boldsymbol{\Omega}_k : \boldsymbol{\Omega}_k = \{\boldsymbol{w}|\boldsymbol{w}\cdot\boldsymbol{w}_k \geqslant 0\} \quad (8)$$

$$\hat{\boldsymbol{w}}_k^{n+1} = \frac{\int_{\boldsymbol{\Omega}_k}\boldsymbol{w}|\hat{\mu}_i(\boldsymbol{w})|^2\mathrm{d}\boldsymbol{w}}{\int_{\boldsymbol{\Omega}_k}|\hat{\mu}_i(\boldsymbol{w})|^2\mathrm{d}\boldsymbol{w}}. \quad (9)$$

Fig. 3 shows the decomposition results of the 2DVMD for $K = 3$, $\alpha = 500$. It is observed that the haze information is all retained in the IMF1, while the high-frequency detail texture is preserved in the IMF2 and IMF3. Therefore, the transmission can be estimated by the IMF1.
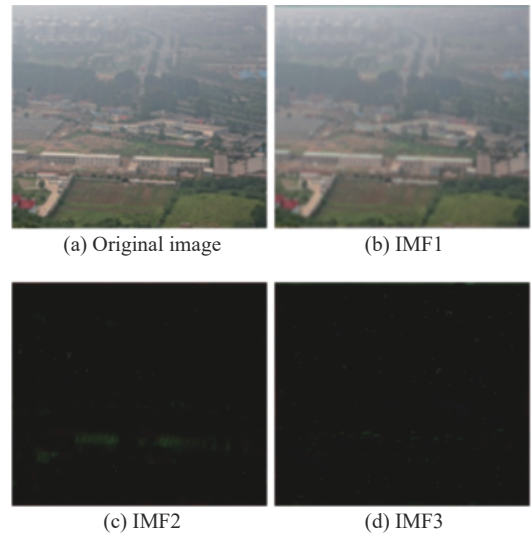

(a) Original image   (b) IMF1

(c) IMF2   (d) IMF3

Fig. 3   Decomposition results of the 2DVMD

2.2 Atmospheric scattering model verification after decomposition

In this section, we need to explain whether the image after the 2DVMD decomposition in this paper meets the atmospheric scattering model, that is, the rationality of the 2DVMD algorithm used in this paper.

We find an interesting phenomenon. As shown in Fig. 4, the two images in the first line are a hazy image and a haze-free image captured in the same sense and the structural similarity index (SSIM) of the two images is 0.27. The two images in the second line are IMF1 of the original images after VMD decomposition and the SSIM is 0.09, which is lower than that of the first line. While the third line are reconstitution images of high frequency IMFs and the SSIM is 0.58, which is higher than that of the first line. SSIM measures the similarity between two images. From a certain point of view, we think that the high-frequency IMF of fog-free images and foggy im-

ages have a high similarity, while the low-frequency IMF has a low similarity because of the influence of haze. We think that we have kept haze in IMF1 as much as possible.
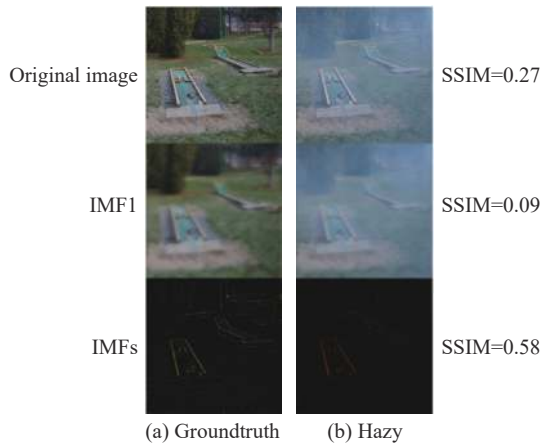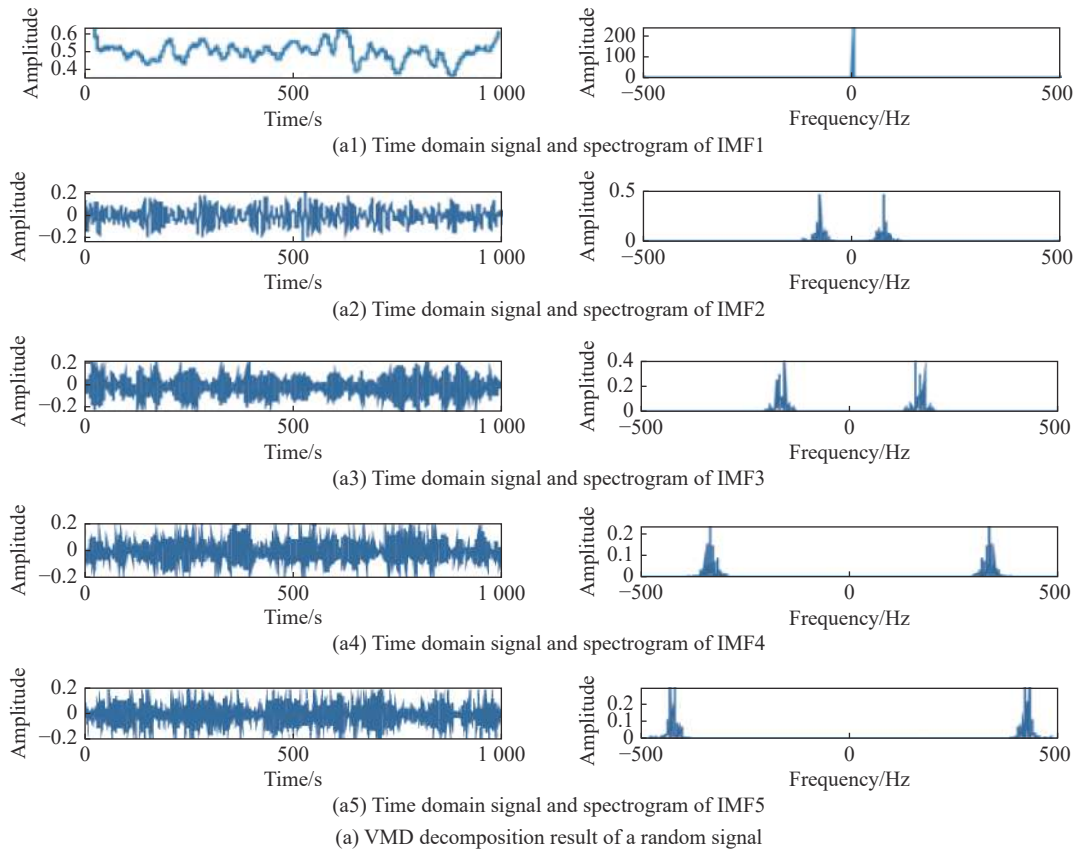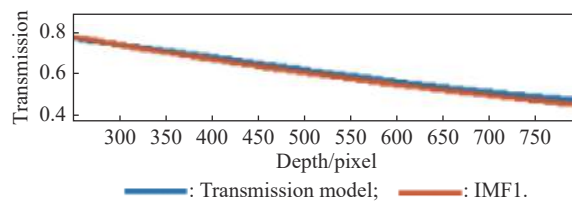

Original image

IMF1

IMFs

SSIM=0.27

SSIM=0.09

SSIM=0.58

(a) Groundtruth   (b) Hazy

Fig. 4   SSIM comparison after VMD decomposition

Fig. 5 (a) is the VMD decomposition result of a piece of random signal. It can be seen from Fig. 5 that after VMD decomposition, the original signal is decomposed into a group of signals with a central frequency and a certain frequency band width, among which IMF1 is a low-frequency signal and the rest IMFs are high-frequency signals. Fattle [16] proposed the atmospheric scattering model and indicated that the transmission was an exponential function of depth of field.

The real scene image can be regarded as approximately continuous or locally continuous, that means the depth of field is linearly changed, the transmittance of depth of field of the linear change is shown in Fig. 5(b), in the blue line, after decomposition of VMD, the IMF1 is obtained as shown in Fig. 5(b) in red line, we can see that the two curves almost overlap and the fit coefficient is $R^2 = 0.992$. As a result, we can see that VMD decomposition does not destroy the atmospheric transmission model.

(a1) Time domain signal and spectrogram of IMF1

(a2) Time domain signal and spectrogram of IMF2

(a3) Time domain signal and spectrogram of IMF3

(a4) Time domain signal and spectrogram of IMF4

(a5) Time domain signal and spectrogram of IMF5

(a) VMD decomposition result of a random signal

: Transmission model;   : IMF1.

(b) VMD decomposition result of the transmission model

Fig. 5   VMD decomposition of atmospheric scattering model

2.3 Low frequency IMF dehazing

Fattal [16] studied the physical models of the atmospheric scattering and the light reflection imaging which is widely applied in computer vision. The IMF1 can be expressed as

$$\boldsymbol{I}_{\mathrm{IMF1}}(x,y) = \boldsymbol{J}_v(x,y)t(x,y) + A(1 - \boldsymbol{t}(x,y)) \qquad (10)$$

where $\boldsymbol{I}_{\mathrm{IMF1}}(x,y)$, A, and $\boldsymbol{J}_v(x,y)$ denote the observed foggy image, global atmospheric light, and the image or scene with no fog reflection, respectively. $t(x,y)$ is the transmission. From (10), we can find that $\boldsymbol{J}_v$ can be obtained by solving $t(x,y)$ and A.

2.4 Transmission estimation

2.4.1 Preliminary estimate of transmittance

He et al. [18] indicated that for some pixels in the local area of the non-sky part of the natural image, at least one of the color channels (R,G,B) has a gray value that approaches 0 which is called dark channel prior (DCP) and it can be expressed as follows:

$$\boldsymbol{J}^{\mathrm{dark}}(x) = \min_{y\in\boldsymbol{\Omega}(x)}\left(\min_{c\in[r,g,b]}\boldsymbol{J}^c(y)\right) \to 0 \qquad (11)$$

where $\boldsymbol{J}^c$ and $\boldsymbol{\Omega}(x)$ are one of the color channels of the image $\boldsymbol{J}$, and the corresponding neighborhood window centered on pixels, respectively.

Here we need to verify whether the image after 2DVMD decomposition still meets the dark channel prior. We select 100 images without haze and sky for statistical analysis, and calculate the dark channel after 2DVMD decomposition. The result shown in Fig. 6(a) and Fig. 6(c) are examples of a haze-free image and its IMF1 after 2DVMD decomposition. Fig. 6(b) and Fig. 6(d) are statistical results of 100 images, average histogram of their original images and average histogram of their IMF1 images. From Fig. 6 we can see that after 2DVMD decomposition, the characteristics of the dark channel of the image does not change substantially, more than 90% of the gray distribution is below 60. Therefore, it can be concluded that after 2DVMD decomposition, the IMF1 image still satisfies the dark channel prior model.

Equation (10) can be rewritten in the following form:

$$\frac{\boldsymbol{I}^c(x,y)}{A^c} = t_o(x,y)\frac{\boldsymbol{J}^c(x,y)}{A^c} + 1 - t_o(x,y). \qquad (12)$$

It is assumed that the transmission value in the neighborhood $\boldsymbol{\Omega}(x)$ is constant, which is recorded as $\hat{t}_o(x)$. Then a DCP operation is conducted on both sides of (10) as follows:

$$\min_{y\in\boldsymbol{\Omega}(x)}\left(\min_{c\in(R,G,B)}\frac{\boldsymbol{I}^c(y)}{A^c}\right) =$$

$$\hat{t}_o(x)\min_{y\in\boldsymbol{\Omega}(x)}\left(\min_{c\in(R,G,B)}\frac{\boldsymbol{I}^c(y)}{A^c}\right) + 1 - \hat{t}_o(x). \qquad (13)$$

(a) Original image

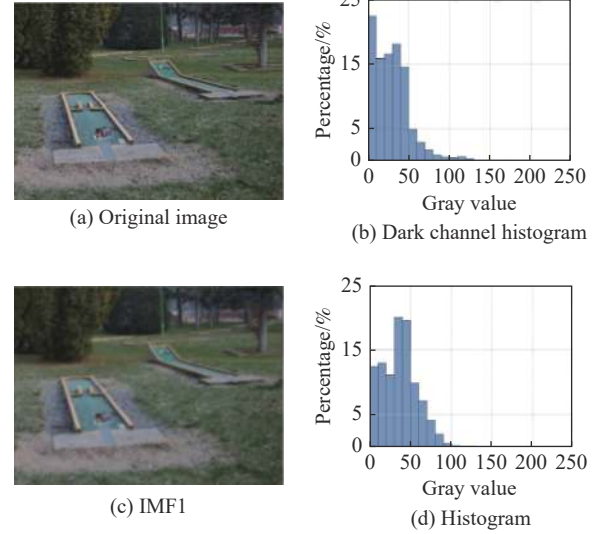(b) Dark channel histogram

(c) IMF1

(d) Histogram

Fig. 6 Drak channel piror model verification

It is assumed that A is constant and $\min_{y\in\boldsymbol{\Omega}(x)}\left(\min_{c\in(R,G,B)}\frac{\boldsymbol{I}^c(y)}{A^c}\right) = 0$. Therefore, the transmission can be roughly estimated with

$$\hat{t}_o(x) = 1 - \min_{y\in\boldsymbol{\Omega}(x)}\left(\min_{c\in(R,G,B)}\frac{\boldsymbol{I}^c(y)}{A^c}\right). \qquad (14)$$

In order to make the images more natural and enhance the corresponding visual effects, it is necessary to retain a part of the atmospheric fog during the image processing. In this regard, the correction factor is set to 0.95.

$$\hat{t}_o(x) = 1 - \lambda\min_{y\in\boldsymbol{\Omega}(x)}\left(\min_{c\in(R,G,B)}\frac{\boldsymbol{I}^c(y)}{A^c}\right) \qquad (15)$$

From (15) we can get the preliminary estimate of the transmittance t_o.

2.4.2 Precise estimation of transmittance

Because this transmittance is not accurate enough, direct use of this transmittance will cause a very serious halo effect. It is necessary to refine it. The transmission can be expressed as follows:

$$\boldsymbol{t}_f(x,y) = \mathrm{e}^{-\mu\boldsymbol{D}(x,y)} \qquad (16)$$

where μ is the scattering coefficient, $\boldsymbol{D}$ is the depth of field. $\boldsymbol{t}_f$ is the precise estimation of transmittance. Equation (16) indicates that the transmission is a function of field depth. Hence, the pixels with the same field depth within the same local area have similar transmission s.

Based on this prior [31], we use the contextual regularization to construct the objective function

$$L = \frac{\lambda}{2} \left\| \boldsymbol{t}_o - \hat{\boldsymbol{t}}_f \right\|_2^2 + \sum_{k \in \Omega} \left\| \boldsymbol{w}_k \circ (\boldsymbol{D}_k \otimes \boldsymbol{t}_o) \right\|_1 \qquad (17)$$

where $\boldsymbol{w}_k$ is a weighting function constructed to approach the difference in transmission between adjacent pixels to zero. $\boldsymbol{D}_k$ is the differential operator, $\otimes$ is the convolution operator, $\circ$ is the Hadmard product.

As Meng et al. [31] mentioned, as the color difference between adjacent elements reduces, the two pixels are more likely to have the same field depth. Therefore, the weighting function can be expressed as follows:

$$\boldsymbol{W}(x,y) = \mathrm{e}^{\frac{-\|\boldsymbol{I}(x)-\boldsymbol{I}(y)\|^2}{2\sigma^2}} \qquad (18)$$

where x and y are two adjacent pixels, and $\|\boldsymbol{I}(x) - \boldsymbol{I}(y)\|$ represents the difference between gray values of adjacent pixels.

The first term of the loss function is the data item, which is applied to measure the fidelity in the transmission optimization process. Moreover, the second term is the correction term, which constrains the correlation between the adjacent transmission. Finally, λ is a regular coefficient for balancing these two terms. It should be indicated that the fine transmission can be obtained by minimizing the loss function.

In order to minimize the loss function, a variable $\boldsymbol{u}_j$ is introduced and the objective function is converted to the form below:

$$\hat{\boldsymbol{t}}_f = \arg\min \frac{\lambda}{2} \left\| \boldsymbol{t}_o - \hat{\boldsymbol{t}}_f \right\|_2^2 + \sum_{j \in w} \left\| \boldsymbol{w}_j \circ \boldsymbol{u}_j \right\|_1,$$

$$\boldsymbol{u}_j = \boldsymbol{D}_j \otimes \boldsymbol{t}_o. \qquad (19)$$

A new loss function can be constructed by using the variable splitting method.

$$f(\boldsymbol{t}_o, \hat{\boldsymbol{t}}_f, \boldsymbol{u}_j) = \frac{\lambda}{2} \left\| \boldsymbol{t}_o - \hat{\boldsymbol{t}}_f \right\|_2^2 + \sum_{j \in w} \left\| \boldsymbol{w}_j \circ \boldsymbol{u}_j \right\|_1 +$$

$$\frac{\beta}{2} \left(\sum_{j \in w} \left\| \boldsymbol{u}_j - \boldsymbol{D}_j \otimes \boldsymbol{t}_o \right\|_2^2 \right) \qquad (20)$$

The accurate transmission can be obtained by minimizing the loss function. In this regard, $\boldsymbol{u}_j$ should be initially determined.

$$\boldsymbol{u}_j = \arg\min \left\| \boldsymbol{w}_j \circ \boldsymbol{u}_j \right\|_1 +$$

$$\frac{\beta}{2} \left(\sum_{j \in w} \left\| \boldsymbol{u}_j - \boldsymbol{D}_j \otimes \boldsymbol{t}_o \right\|_2^2 \right) =$$

$$\max \left(\left| \boldsymbol{D}_j \otimes \boldsymbol{t}_o \right| - \frac{\boldsymbol{W}_j}{\beta}, 0 \right) \cdot \mathrm{sign}(\boldsymbol{D}_j \otimes \boldsymbol{t}_o) \qquad (21)$$

Then, $\hat{\boldsymbol{t}}_f$ is determined.

$$\hat{\boldsymbol{t}}_f = \arg\min \frac{\lambda}{2} \left\| \boldsymbol{t}_o - \hat{\boldsymbol{t}}_f \right\|_2^2 +$$

$$\frac{\beta}{2} \left(\sum_{j \in w} \left\| \boldsymbol{u}_j - \boldsymbol{D}_j \otimes \boldsymbol{t}_o \right\|_2^2 \right) \qquad (22)$$

Fig. 7 shows the results of the transmission estimation outcome. The algorithm in this paper is compared with the algorithm by He et al. [18]. From top to bottom are the original image containing fog, the estimated transmittance of the two algorithms, the image defogging results and the local amplification results of the image in the red rectangle. It is obvious, according to the partial enlarged image that the result processed by the algorithm proposed by He et al. has a loss of information, while the algorithm in this paper achieves a stronger contrast and retains more details. The proposed algorithm can estimate the transmission more accurately in comparison with He's algorithm [19]. Besides, it can reflect the depth information of the images.
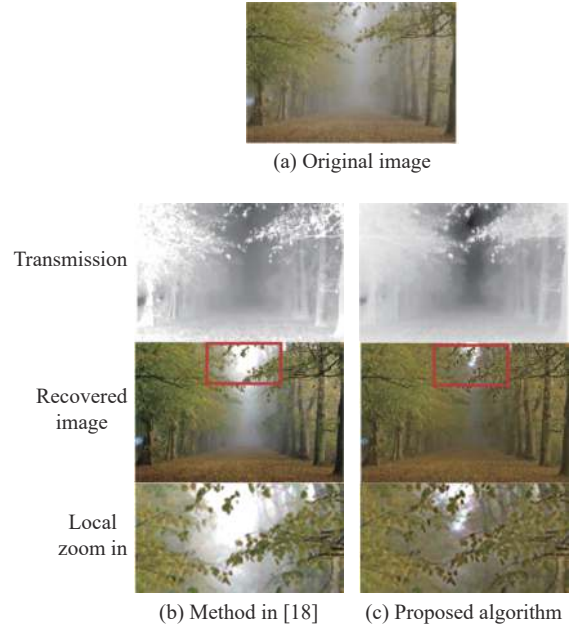

(a) Original image

Transmission

Recovered image

Local zoom in

(b) Method in [18]   (c) Proposed algorithm

Fig. 7   Results of the transmission estimation, obtained from different algorithms

2.5   Atmospheric light evaluation

Equation (10) indicates that the selection of the atmospheric light directly determines the brightness of the restored images. The method proposed by He et al. [18] was based on the maximum value of pixels in the fog images corresponding to the top 0.1% of the pixels in the dark channel images as the global atmospheric light in-

tensity value. The selected atmospheric light by the method generally has a high brightness value so that the recovered images will be dark in accordance with (10). The present study investigates the idea of [32], which claims that the part of the sky area with a lower brightness value is regarded as the atmospheric light. The application of this technique increases the brightens of the obtained images and improves the corresponding visual effects.

Sky has a high brightness value and a slow variation rate in terms of the gradation value, and it is located at the top of the normal photograph. Therefore, the image gray values are combined with the brightness and the position information to perform the sky area segmentation.

For images containing the sky, the Otsu method is applied to the process. Then morphological opening and closing operations are conducted to manipulate images. Finally, the top region is identified as the sky. In order to reduce the adverse impact of the noise on the method performance, the first 0.5% of the pixels with the lowest sky brightness is eliminated. Then the minimum brightness is taken as the global atmospheric light.

For non-sky images, a quadtree search method is adopted to evaluate the atmospheric light. Based on this evaluation, the input images are divided into four squares. Then the difference between the pixel average and the standard deviation of each square is calculated as the score, where the area with the highest score is selected to be divided into another four squares. The process is repeated until the square area is smaller than the set threshold. Then the brightest value is considered as the global atmospheric light. Fig. 8 shows the estimation results for the global atmospheric light.
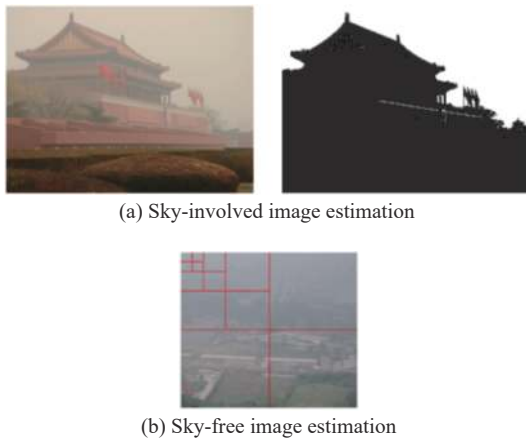

(a) Sky-involved image estimation

(b) Sky-free image estimation

Fig. 8   Estimation results for global atmospheric lights

2.6   Recovery of haze-free image

From (10) we can get that

$$J_v(x,y) = \frac{I_{\mathrm{IMF1}}(x,y) - A(1 - t(x,y))}{t(x,y)}. \quad (23)$$

From the sections above, we can obtain refined transmittance t_f, and atmospheric light A. To avoid a divide by zero exception, we revise (23) as

$$J_v(x,y) = \frac{I_{\mathrm{IMF1}}(x,y) - A(1 - t_f(x,y))}{\max(t(x,y), 0.1)}. \quad (24)$$

Therefore, the final recovered haze-free image can be expressed as

$$J = \frac{I_{\mathrm{IMF1}}(x,y) - A(1 - t_f(x,y))}{\max(t(x,y), 0.1)} + I_{\mathrm{IMF2}} + I_{\mathrm{IMF2}} + \cdots + I_{\mathrm{IMF}n}. \quad (25)$$

3. Experiment

Firstly, we conduct experiments to explore the influence of parameters in 2DVMD on the results of dehazing. Then, we conduct experiments to compare our proposed algorithm with the state-of-art algorithms to verify the effectiveness of our proposed algorithm. Meanwhile, we chose some commonly used indicators for further objective comparison of the performance of the algorithms.

3.1   Impacts of VMD parameters on dehazing effect

3.1.1   Impacts of mode number K on dehazing effect

In our proposed algorithm, the value of K and α has certain influence on the result of defogging. As the value of K parameter increases, the VMD decomposition theory indicates that the frequency difference between modes is becoming increasingly smaller, which means that the components of the fog may not be included in the basic IMF.

When we set $\alpha = 2\,000$, K increases from 2 to 17, and the images are processed respectively. Fig. 9 shows some results that $K = 2, 3, 7, 8, 9$. It is observed that as the value of K increases, the contrast of the dehazing result tends to increase. However, when the K value is too large, color distortion and over-brightness will occur. Furthermore, the Brisque, SSIM, peak signal to noise ratio (PSNR), and entropy indicators are applied. The lower the Brisque index is, the higher the image quality can be. The higher the other indicators are, the better the image quality can be. In addition, Fig. 10 indicates that the value of the Brisque decreases initially and then increases rapidly as the value of K increases. When $K = 8$, the Brisque reaches the smallest value. Moreover, the SSIM value decreases as K increases. The PSNR decreases first, and then increases and finally decreases. Furthermore, the entropy first increases and then decreases and when $K = 8$ the maximum entropy is obtained.
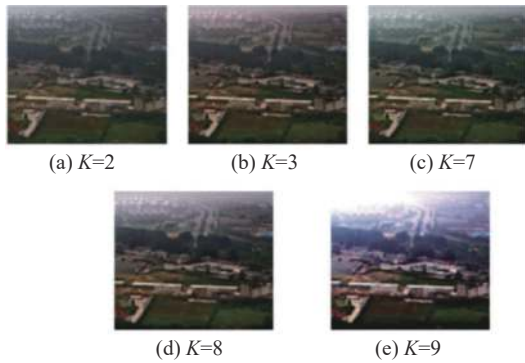
(a) K=2   (b) K=3   (c) K=7

(d) K=8   (e) K=9

Fig. 9   Influence of the parameter K on the result of dehazing

(a) Brisque
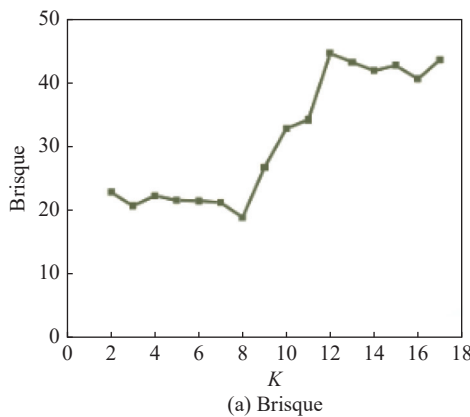

(b) SSIM

(c) PSNR

(d) Entropy

Fig. 10   Quantitative analysis of influence of parameter K on the result of dehazing

3.1.2   Impacts of the penalty factor α on dehazing results

From Fig. 11 and Fig. 12 we can see that compared with K, α value has little effect on the dehazing result. According to the entropy index and the Brisque index, the best effect occurs when $\alpha = 2\,500$. Moreover, according to PSNR and SSIM, the best effect occurs when $\alpha = 4\,300$.

We can use the particle swarm optimization (PSO) algorithm to search the optimal combination of K and α. However, the algorithm still has the problem of too much computation. This method can be used in the case demanding high precision but without requirements for calculation time and real time. If there is a requirement for calculation time, appropriate parameters can be selected according to experiential judgment. In general, setting $K \in [3, 5]$ and $\alpha \in [2\,000, 5\,000]$ is likely to lead to better results.
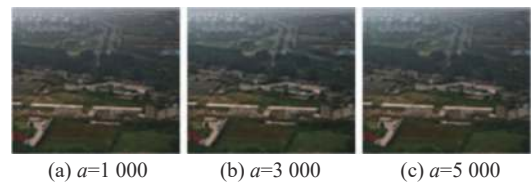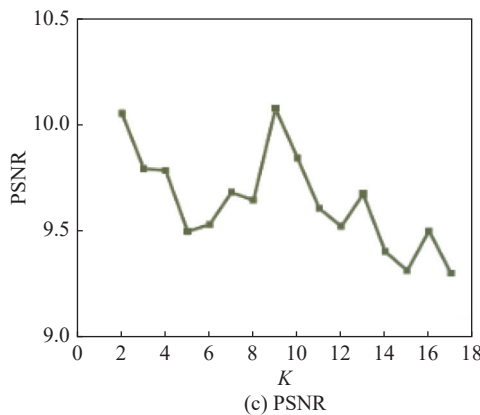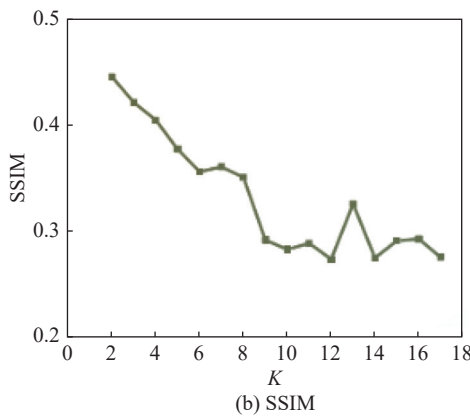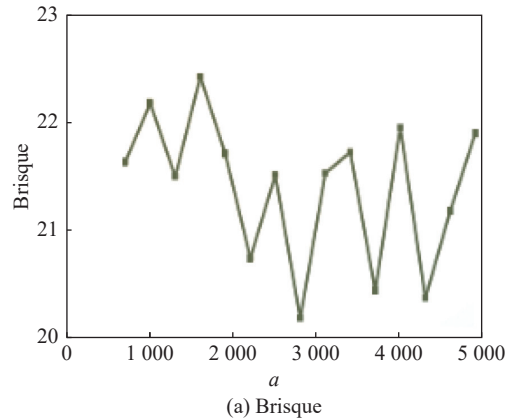

(a) a=1 000   (b) a=3 000   (c) a=5 000

Fig. 11   Influence of parameter α on the result of dehazing

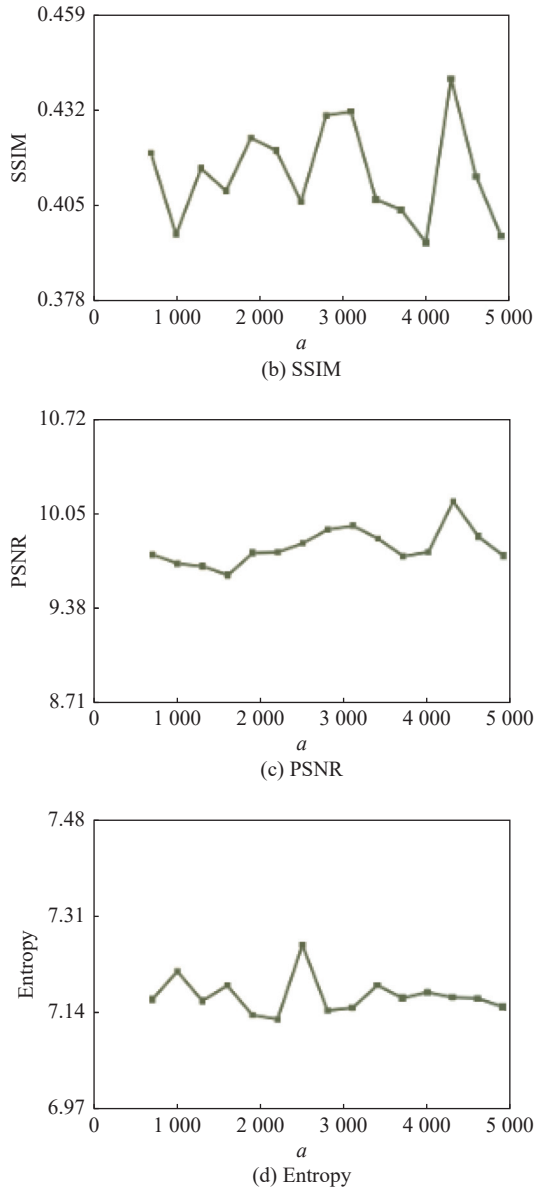(a) Brisque

(b) SSIM

(c) PSNR

(d) Entropy

Fig. 12   Quantitative analysis of influence of parameter α on the result of dehazing

3.2   Dehazing performance of the proposed method

The experiments are conducted on a computer with a 2.7 GHz Inter-Core CPU, 8 GB RAM. The software platform is Matlab 2017a. We use four objective evaluation factors which are PSNR, SSIM, Brisque and Entropy to compare the performance of the algorithms.

3.2.1   Objective evaluation factors

The PSNR reflects the ratio of the maximum signal volume to the noise intensity. It is found that the higher the value, the better the image quality. The calculation equation is described as follows:

$$PSNR = 10 \lg \left(\frac{A^2}{\frac{1}{M \times N} \left[\sum_{i=0}^{M} \sum_{j=0}^{N} (f_{ij} - g_{ij})^2 \right]} \right). \qquad (26)$$

The SSIM measures the image similarity from different aspects, including the brightness, contrast, and the structure. It is found that as the structural similarity index increases, the image distortion decreases.

$$SSIM(x, y) = \frac{(2\mu_x \mu_y + C_1)(2\sigma_x \sigma_y + C_2)}{(\mu_x^2 + \mu_y^2 + C_1)(\sigma_x^2 + \sigma_y^2 + C_2)} \qquad (27)$$

The Brisque index is a non-reference image quality evaluation model based on the versatility of natural scene statistics. The scene statistical model is applied to quantize the image quality, where localized normalized brightness coefficients are utilized in this regard. The SVM model parameters with different distortion types are used to train the hyperplane corresponding to different distortion types. The final quality score [33] can be obtained by the probability and quality corresponding to different distortion types.

3.2.2   Qualitative comparison

To verify the effectiveness of the proposed dehazing approach, it is tested on various types of hazy images. The performance of the proposed method is compared with that of various state-of-the-art dehazing methods: the multi-scale correlated wavelet approach (MSCWA) [34], deep features image net (DFIN) method [35], artificial multiple-exposure (AME) method [36], saturation based transmission map estimation (SBTME) method [37], low-pass polarization filter (LPPF) method [38], approximating and eliminating airlight component (AEAC) method [39], airlight refinement and non-linear color balancing (ARNCB) method [40], lower bound non-linear bounding function (LBBF) method [41], improved color attenuation prior (ICAP) method [42], and atmospheric light fusion (ALF) method [43].

The end-to-end dehazing results on challenging natural images are presented. Fig. 13 ~ Fig. 17 show a qualitative comparison of our results with those of ten state-of-the-art dehazing methods.

MSCWA results in poor robustness, as we can see from Fig.13 to Fig.17 that the dehazing effect of Image 1 is relatively good, but the visual effect of Image 2 is poor with low contrast and color shift especially in the background region. DFIN is an algorithm based on deep learning, the overall performance of the method is better, but the performance will be affected by the training dataset and the fog in the distance is not cleaned up in Image 2

and Image 4. The AME algorithm cannot accurately restore the details of the image, resulting in low contrast. The overall color of the result obtained by the SBTME algorithm is dark and the details in the distance cannot be restored accurately as we can see in Image 2 and Image 5. The result of LPPF has certain halos and artifacts and the fog is not completely removed, for example, the fog in the distance of Image 1, and some parts of Image 2 are white due to the fog not being removed, partly because the transmittance estimation is inaccurate. The AEAC algorithm darkens the results, as we can see from Image 3 that the road is dark and halos and artifacts appear in Image 4 at the edge of the plants. ARNCB results in color over saturated, the road in Image 2 looks unnatural and

appears unnatural patches, and details of the image are partially overestimated. LBBF generates halo artifacts near discontinuities as we can see in Image 4. ALF algorithms do not completely remove fog, and the dehazing performance is bad. The ICAP algorithm has certain artifacts, color shift occurs in Image 2, and the recovery effect at long distances is not good, resulting in the loss of details. For Image 5, due to the uneven thickness of fog, all kinds of algorithms are difficult to remove the fog clean, but the algorithm in this paper retains the image details to the greatest extent and has the best visual effect. The proposed algorithm has competitive results with these methods, producing a better dehazed image with controlled brightness, contrast, and more details.
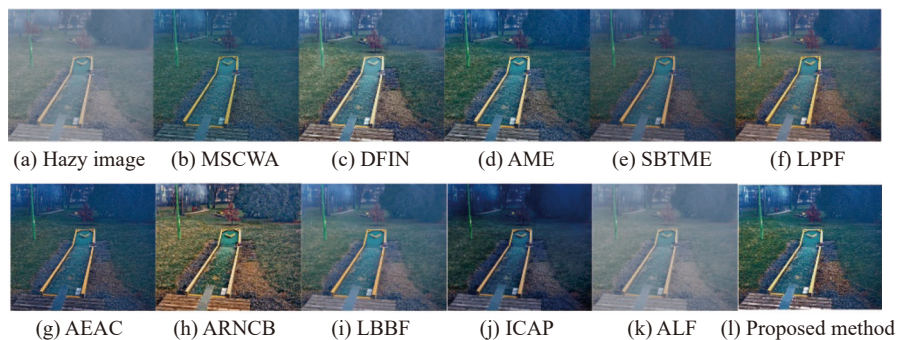

(a) Hazy image　(b) MSCWA　(c) DFIN　(d) AME　(e) SBTME　(f) LPPF

(g) AEAC　(h) ARNCB　(i) LBBF　(j) ICAP　(k) ALF　(l) Proposed method

Fig. 13　Performance comparison of signal Image 1 dehazing methods using sample natural images

(a) Hazy image　(b) MSCWA　(c) DFIN　(d) AME　(e) SBTME　(f) LPPF

(g) AEAC　(h) ARNCB　(i) LBBF　(j) ICAP　(k) ALF　(l) Proposed method
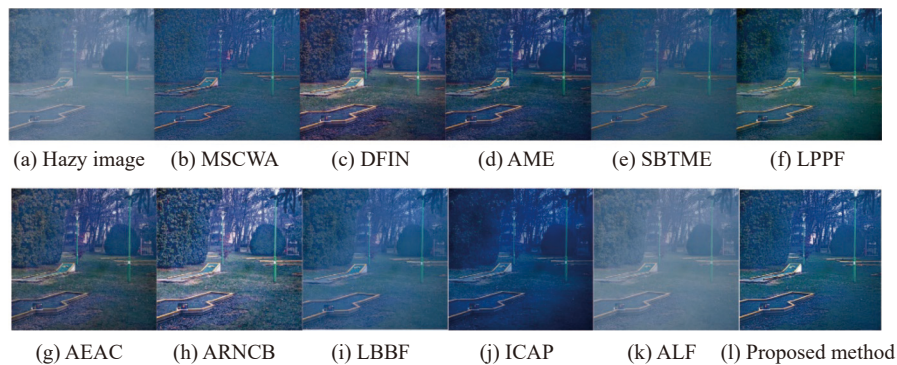
Fig. 14　Performance comparison of signal Image 2 dehazing methods using sample natural images

(a) Hazy image　(b) MSCWA　(c) DFIN　(d) AME　(e) SBTME　(f) LPPF

(g) AEAC　(h) ARNCB　(i) LBBF　(j) ICAP　(k) ALF　(l) Proposed method
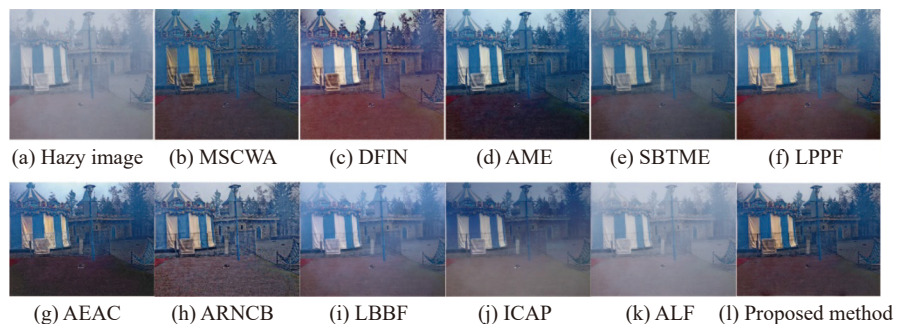
Fig. 15　Performance comparison of signal Image 3 dehazing methods using sample natural images

(a) Hazy image   (b) MSCWA   (c) DFIN   (d) AME   (e) SBTME   (f) LPPF

(g) AEAC   (h) ARNCB   (i) LBBF   (j) ICAP   (k) ALF   (l) Proposed method
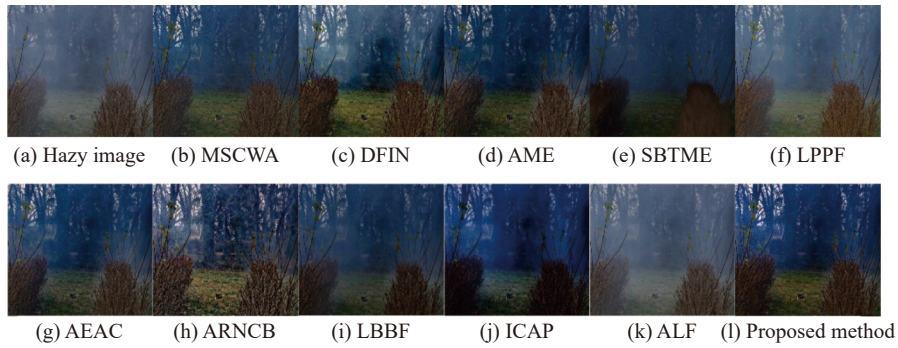
Fig. 16   Performance comparison of signal Image 4 dehazing methods using sample natural images

(a) Hazy image   (b) MSCWA   (c) DFIN   (d) AME   (e) SBTME   (f) LPPF

(g) AEAC   (h) ARNCB   (i) LBBF   (j) ICAP   (k) ALF   (l) Proposed method
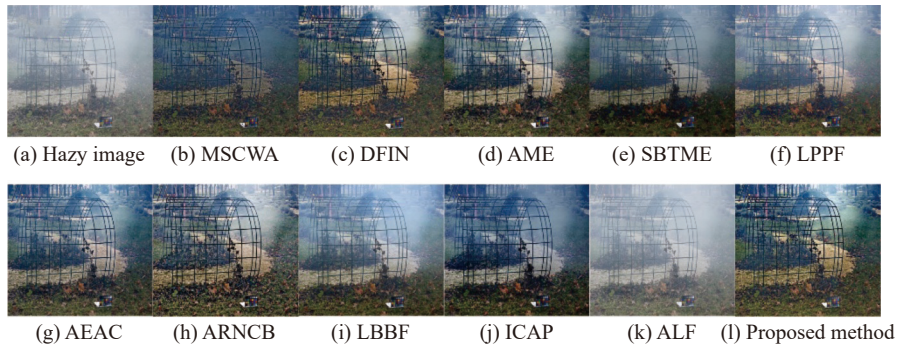
Fig. 17   Performance comparison of signal Image 5 dehazing methods using sample natural images

Fig. 18 presents the comparison of our results with those of 10 state-of-the-art dehazing methods on real unmanned aerial vehicle (UAV) sample images. These images all contain the sky, which is difficult to deal with, especially for Image 1, most of the algorithms are oversaturated, and there is a serious color shift in the sky region. The results of MSCWA overestimate the sky, and the sky area effect is poor, resulting in low contrast. The results of DFIN in Image 2 is dark and the contrast is low. AME results in detail loses especially in Image 1, the mountain in the long distance. SBTME results in bad color shift as in Image 1. LPPF loses the image details in Image 2. AEAC over-enhances the sky in Image 2. ARNCB does not remove the fog cleanly in Image 4. LBBF results in low contrast. ICAP results in serious color shift in Image 1. ALF algorithms do not completely remove fog, and the dehazing performance is bad. In comparison, the proposed method effectively recovers the image details and removes fog.

3.2.3   Quantitative comparison

In this paper, the outdoor dataset O-HAZE as shown in Fig. 11 is exploited to quantify the dehazing performance of different algorithms. Ancuti et al. [44] built the datasets, where hazy images have been captured in presence of real haze, generated by professional haze machines, and O-HAZE contains 45 different outdoor scenes depicting the same visual content recorded in haze-free and hazy conditions, under the same illumination parameters.
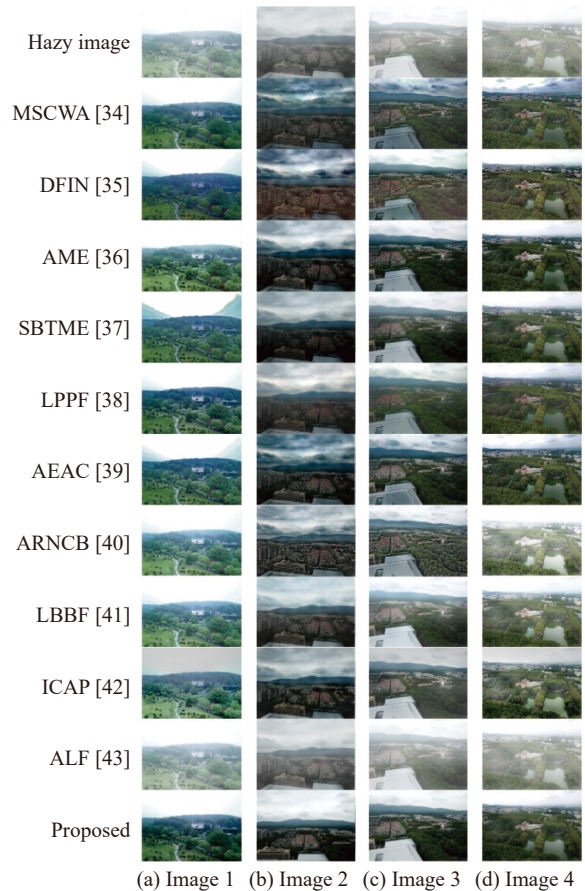

(a) Image 1   (b) Image 2   (c) Image 3   (d) Image 4

Fig. 18   Performance comparison of various single image dehazing methods using sample real UAV images

Table 1 presents the average performance of those algorithms in terms of the PSNR, SSIM, Brisque, entropy and running time. The top three performances are highlighted in red, blue and purple, as we can see from the table that our algorithm has the best PSNR, SSIM and entropy and has the second highest Brisque and running time. PSNR and entropy index in some extent, reflect the image contrast, and the results are consistent with the subjective evaluation. The results of SSIM show the defogging results obtained by the algorithm in this paper with the highest similarity with the groundtruth, reflecting its fogging results are better. Brisque is a no-reference indicator, its evaluation is from studying a lot of natural images and it is not very sensitive to contrast of the image, so the algorithm in this paper achieves the second score. The state-of-the-art deep learning defogging method usually needs a lot of training data set and calculation parameters, therefore they do not have too much advantage in terms of running speed under the condition of certain computing resources. The algorithm in this paper also achieves the second performance in terms of running speed because this article needs certain iteration during 2DVMD decomposition. We can find that our method achieves the best performance on the whole.

Table 1   Quantitative comparisions of various algorithms

Algorithm	PSNR	SSIM	Brisque	Entropy	Running time/s
MSCWA	17.41	0.8112	22.53	6.93	1.73
DFIN	19.32	0.9052	10.12	7.07	3.11
AME	20.18	0.9034	17.5	7.12	2.14
SBTME	23.21	0.901	10.98	7.53	4.30
LPPF	20.12	0.8918	19.2	7.41	1.17
AEAC	20.86	0.8945	15.3	7.26	1.35
ARNCB	20.52	0.8237	15.8	7.17	0.91
LBBF	22.23	0.9009	10.87	7.49	1.86
ICAP	20.17	0.88125	14.2	7.19	0.99
ALF	18.64	0.7938	20.1	6.98	1.22
Proposed algorithm	23.24	0.917	10.13	7.62	0.93

4. Conclusions

The imaging equipment quality can be affected by outdoor haze conditions, which results in low contrast and poor visibility, while single image dehazing has been a challenge because of its ill-posed nature. This paper aims to provide a method of dehazing to preserve image details. We find that the frequency components of images polluted by haze will become lower, and the frequency components of images are mostly concentrated in the low-frequency part, while the high-frequency distribution is very small. Thus, the basic idea of this paper is to extract

the low frequency components of the hazy images. The haze information is contained in the low-frequency components and the detailed texture information is included in the high frequency components. Therefore, we restore the low frequency components and then fuse with the high frequency parts and finally get a high contrast and good visual effect processing results. The 2DVMD method is used to adaptively decompose images into low-frequency and high-frequency images according to the image frequency band. Furthermore, we optimize the atmospheric light and transmittance estimation method to obtain a defogging effect with richer details and higher contrast. The proposed method is compared with ten state-of-the-art algorithms respectively, namely, MSCWA, DFIN, AME, SBTME, LPPF, AEAC, ARNCB, LBBF, ICAP, and ALF on the O-HAZE dataset and the real UAV images and PSNR, SSIM, Brisque and entropy are used as objective evaluation factors. Experiment results show that the proposed algorithm has competitive results with these methods, producing a better dehazed image with controlled brightness, contrast, and more details.

References

[1] SCHECHNER Y Y, NARASIMHAN S G, NAYAR S K. Instant dehazing of images using polarization. Proc. of the IEEE Conference on Computer Vision & Pattern Recognition, 2001. DOI: 10.1109/CVPR.2001.990493.

[2] SHAO X, FEI L P, LIN W. Dehazing method through polarimetric imaging and multi-scale analysis. Proc. of the SPIE Sensing Technology + Applications, 2015: 266–273.

[3] QU Y F, ZOU Z F. Non-sky polarization-based dehazing algorithm for non-specular objects using polarization difference and global scene feature. Optics Express, 2017, 25(21): 25004.

[4] SHWARTZ S, NAMER E, SCHECHNER Y Y. Blind haze separation. Proc. of the IEEE Computer Society Conference on Computer Vision & Pattern Recognition, 2006: 1984–1991.

[5] MIYAZAKI D, AKIYAMA D, BABA M, et al. Polarization-based dehazing using two reference objects. Proc. of the IEEE International Conference on Computer Vision, 2013: 852–859.

[6] RONG Z, WANG L J. Improved wavelet transform algorithm for single image dehazing. Optik-International Journal for Light and Electron Optics, 2014, 125(13): 3064–3066.

[7] ZHANG H, LIU X, HUANG Z T, et al. Single image dehazing based on fast wavelet transform with weighted image fusion. Proc. of the IEEE International Conference on Image Processing, 2014: 4542–4546.

[8] XIE C H, QIAO W W, ZHANG X X, et al. Single image dehazing algorithm using wavelet decomposition and fast kernel regression model. Journal of Electronic Imaging, 2016, 25(4): 043003.

[9] XIAO C X, GAN J J. Fast image dehazing using guided joint bilateral filter. Visual Computer, 2012, 28(6/8): 713–721.

[10] SERIKAWA S, LU H M. Underwater image dehazing using joint trilateral filter. Computers & Electrical Engineering,

2014, 40(1): 41–50.

[11] SUN K, WANG B, ZHENG Z Z, et al. Fast single image dehazing using iterative bilateral filter. Proc. of the International Conference on Information Engineering & Computer Science, 2010. DOI: 10.1109/ICIECS.2010.5678374.

[12] SHRIVASTAVA A, JAIN S. Single image dehazing based on one dimensional linear filtering and adoptive histogram equalization method. Proc. of the International Conference on Electrical, Electronics, and Optimization Techniques, 2016: 4074–4078.

[13] GALDRAN A, ALVAREZ A, BRIA A, et al. On the duality between Retinex and image dehazing. Proc. of the IEEE/CVF Conference on Computer Vision and Pattern Recognition, 2018: 8212–8221.

[14] XIE B, FAN G, CAI Z X. Improved single image dehazing using dark channel prior and multi-scale Retinex. Proc. of the International Conference on Intelligent System Design and Engineering Application, 2010: 848–851.

[15] ZHOU J J, ZHOU F G. Single image dehazing motivated by Retinex theory. Proc. of the 2nd International Symposium on Instrumentation and Measurement, Sensor Network and Automation, 2013: 243–247.

[16] FATTAL R. Single image dehazing. ACM Transactions on Graphics, 2008, 27(3): 1–9.

[17] TAN R T. Visibility in bad weather from a single image. Proc. of the IEEE Conference on Computer Vision and Pattern Recognition, 2008. DOI: 10.1109/CVPR.2008.4587643.

[18] HE K M, SUN J, TANG X O. Single image haze removal using dark channel prior. IEEE Trans. on Pattern Analysis and Machine Intelligence, 2011, 33(12): 2341–2353.

[19] HE K M, SUN J, TANG X. Guided image filtering. Proc. of the European Conference on Computer Vision, 2010. DOI:10.1007/978-3-642-15549-9_1.

[20] TAREL J, HAUTIERE N. Fast visibility restoration from a single color or gray level image. Proc. of the IEEE 12th International Conference on Computer Vision, 2009: 2201–2208.

[21] WANG J B, HE N, ZHANG L L, et al. Single image dehazing with a physical model and dark channel prior. Neurocomputing, 2015, 149: 718–728.

[22] HUANG C Q, YANG D, ZHANG R L, et al. Improved algorithm for image haze removal based on dark channel priority. Computers & Electrical Engineering, 2018, 70: 659–673.

[23] PENG Y T, CAO K M, COSMAN P C. Generalization of the dark channel prior for single image restoration. IEEE Trans. on Image Processing, 2018, 27(6): 2856–2868.

[24] WANG Z, HOU G J, PAN Z K, et al. Single image dehazing and denoising combining dark channel prior and variational models. IET Computer Vision, 2018, 12(4): 393–402.

[25] SUAREZ P L, SAPPA A D, VINTIMILLA B X, et al. Deep learning based single image dehazing. Proc. of the IEEE/CVF Conference on Computer Vision and Pattern Recognition Workshops, 2018: 1169–1176.

[26] SANTRA S, MONDAL R, CHANDA B. Learning a patch quality comparator for single image dehazing. IEEE Trans. on Image Processing, 2018, 27(9): 4598–4607.

[27] CAI B L, XU X M, JIA K, et al. Dehazenet: an end-to-end system for single image haze removal. IEEE Trans. on Image Processing, 2016, 25(11): 5187–5198.

[28] REN W Q, LIU S, ZHANG H, et al. Single image dehazing via multi-scale convolutional neural networks. Proc. of the European Conference on Computer Vision, 2016: 154–169.

[29] LI B Y, PENG X L, WANG Z Y, et al. Aod-net: all-in-one dehazing network. Proc. of the IEEE International Conference on Computer Vision, 2017: 4770–4778.

[30] DRAGOMIRETSKIY K, ZOSSO D. Two-dimensional variational mode decomposition. Journal of Mathematical Imaging and Vision, 2017, 58(2): 294–320.

[31] MENG G F, WANG Y, DUAN J Y, et al. Efficient image dehazing with boundary constraint and contextual regularization. Proc. of the International Conference on Computer Vision, 2013: 617–624.

[32] LIU C X, SHEN Y Y, SHAO Y Q, et al. Sky detection- and texture smoothing-based high-visibility haze removal from images and videos. Computer Animation and Virtual Worlds, 2017, 28(3/4): e1776.

[33] SUN T, ZHU X J, PAN J S, et al. No-reference image quality assessment in spatial domain. Advances in Intelligent Systems and Computing, 2015: 381–388.

[34] LIU X, ZHANG H, CHEUNG Y M, et al. Efficient single image dehazing and denoising: an efficient multi-scale correlated wavelet approach. Computer Vision and Image Understanding, 2017, 162: 23–33.

[35] XU Z, YANG X T, LI X, et al. The effectiveness of instance normalization: a strong baseline for single image dehazing. https://arxiv.org/abs/1805.03305.

[36] GALDRAN A. image dehazing by artificial multiple-exposure image fusion. Signal Processing, 2018, 149: 135–147.

[37] KIM S E, PARK T H, EOM I K. Fast single image dehazing using saturation based transmission map estimation. IEEE Trans. on Image Processing, 2020, 29: 1985–1998.

[38] AMER K O, ELBOUZ M, ALFALOU A, et al. Enhancing underwater optical imaging by using a low-pass polarization filter. Optics Express, 2019, 27(2): 621–643.

[39] BORKAR K, MUKHERJEE S. Single image dehazing by approximating and eliminating the additional airlight component. Neurocomputing, 2020, 400: 294–308.

[40] DHARA S K, ROY M, SEN D, et al. Color cast dependent image dehazing via adaptive airlight refinement and non-linear color balancing. IEEE Trans. on Circuits and Systems for Video Technology, 2020, 31(5): 2076–2081.

[41] RAIKWAR S C, TAPASWI S. Lower bound on transmission using non-linear bounding function in single image dehazing. IEEE Trans. on Image Processing, 2020, 29: 4832–4847.

[42] KANSAL I, KASANA S S. Improved color attenuation prior based image de-fogging technique. Multimedia Tools and Applications, 2020, 79(17/18): 12069–12091.

[43] HAJJAMI J, NAPOLEON T, ALFALOU A. Efficient sky dehazing by atmospheric light fusion. Sensors, 2020, 20(17): 4893.

[44] ANCUTI C O, ANCUTI C, TIMOFTE R, et al. O-HAZE: a dehazing benchmark with real hazy and haze-free outdoor images: NTIRE. Proc. of the IEEE Conference on Computer Vision and Pattern Recognition Workshops, 2018: 754–762.

Biographies

QIN Chaoxuan was born in 1991. He received his B.S. degree from the School of Mechanical Engineering, Nanjing University of Science and Technology, Nanjing, China, in 2014. He received his Ph.D. degree from the School of Mechanical Engineering, Nanjing University of Science and Technology, China, in 2021. He is currently working as an engineer with the Southwest Technology and Engineering Research Institute. His current research interests focus on computer vision, signal processing, and target identification.
E-mail: qinchaoxuan1991@163.com

GU Xiaohui was born in 1964. He received his Ph.D. degree from the School of Mechanical Engineering, Nanjing University of Science and Technology, China in 2002. He is a professor and a doctoral supervisor at the School of Mechanical Engineering, Nanjing University of Science and Technology, China. His research interests include computer vision, artificial intelligence, and reliability engineering.
E-mail: gxiaohui@njust.edu.cn